JOURNAL OF SOLID STATE CHEMISTRY 76, 248–259 (1988)

3.1 GeV–Xenon Ion Latent Tracks in $Bi_2Fe_4O_9$: Mössbauer and Electron Microscopy Studies*

D. GROULT, M. HERVIEU, N. NGUYEN, AND B. RAVEAU

Laboratoire de Cristallographie et Sciences des Matériaux, ISMRA, Boulevard du Maréchal Juin, 14032 Caen Cedex, France

Received July 15, 1987; in revised form October 30, 1987

3.1 GeV–xenon ions irradiation effects induced in bismuth iron oxide $Bi_2Fe_4O_9$ have been investigated by Mössbauer spectroscopy and electron microscopy. The amorphization of the crystalline compound achieved for a fluence close to 5×10^{12} cm^{-2} has been interpreted on the basis of a track mechanism with a damage rate expressed as $Fd = 1 - \exp(-\pi R^2 \phi t)$ where R is the track radius.

Introduction

The study of highly energetic heavy ion effects in magnetic oxides has been carried out at the heavy ion accelerator GANIL in Caen for the past 3 years. It has been shown from magnetic measurements (*1–2*), Mössbauer spectroscopy (*3–4*), and high resolution electron microscopy (*5–8*) that changes in microstructure and magnetic properties are caused by a defect mechanism which is very similar for 1.8 GeV–Ar and 2.7 GeV–Kr ions but different for 3.1 GeV–Xe ions. For the former the mechanism is mainly based on nuclear stopping whereas for Xe ions it is related to electronic stopping. However, even for Ar and Kr ions, the enhancement of the damage rate by inelastic collisions has been clearly demonstrated (*9–10*).

These results lead us to assume that a pure track mechanism can be expected whenever the energy deposited by electronic stopping reaches a threshold value which has been estimated to be about 17 MeV cm^2 mg^{-1} for $Y_3Fe_5O_{12}$, 22 MeV cm^2 mg^{-1} for $BaFe_{12}O_{19}$, and 26 MeV cm^2 mg^{-1} for $NiFe_2O_4$.

The bismuth iron ferrite $Bi_2Fe_4O_9$ is an attractive candidate for such a study because of its mixed framework built up of FeO_6 octahedra and FeO_4 tetrahedra like garnets, and also like barium hexaferrite. Moreover this oxide exhibits a lower packing density than yttrium iron garnet and barium hexaferrite and spinels which are close packed structures. Thus the influence of atomic density criterion may be investigated in the response of insulators to irradiation. In particular, the track formation mechanism is interesting. The first part of this work has been devoted to a Mössbauer study of the radiation effects of 3.1 GeV–xenon ions together with the investigation of the induced microstructural changes using transmission electron microscopy.

* Experiment performed at the National Laboratory GANIL with the collaboration of CIRIL, Caen, France.

0022-4596/88 $3.00

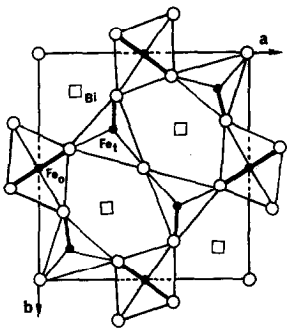

FIG. 1. Schematic drawing of the structure of $Bi_2Fe_4O_9$ down to (001).

During this investigation the existence of latent tracks has been demonstrated. The structural study of such tracks by high resolution electron microscopy which corresponds to the second part of this work will be published in a later paper.

Experimental

$Bi_2Fe_4O_9$ samples have been irradiated with xenon ions of a specific energy E/m = 24 MeV/amu (E = 3.1 GeV, m = 129 amu) at the heavy ion accelerator GANIL. Disks 3 mm in diameter were cut from sintered polycrystalline samples prepared by conventional ceramic techniques and piled up normal to the ion beam. As noted elsewhere (*1–2*), the thickness of the disks takes into account the mean projected range of the 3.1 GeV–Xe ions, namely, Rp = 200 μm.

The ^{57}Fe Mössbauer spectra were recorded at 295 K using the standard absorption method with a constant acceleration spectrometer and ^{57}Co in Rh source. The emitted γ-rays were collimated by a hole drilled in a 5-mm-thick lead disk and placed at a distance of 100 mm from the source. The electron diffraction study was carried out with a JEOL 100 CX electron microscope supplied with a side entry goniometer (±60°). Microstructural changes induced by the incoming ions were studied using a JEOL 200 CX HREM electron microscope fitted with a top-entry goniometer (±10°). Small microcrystals of the irradiated disks were collected on copper supported holey carbon films after splitting in liquid nitrogen to avoid any mechanical effects.

Results

Mössbauer Spectroscopy

The structure of $Bi_2Fe_4O_9$ (*11*) can be described as formed of isolated rutile chains of FeO_6 octahedra linked by Fe_2O_7 tetrahedral groups (Fig. 1). The bismuth ions are surrounded by eight oxygen ions. The Fe^{3+} ions are distributed evenly between the tetrahedral and octahedral positions so that the formula may be written $Bi_2Fe_2^{(T)}Fe_2^{(O)}O_9$. Such a distribution leads to a Mössbauer spectrum which shows at 295 K three peaks of different intensities (Fig. 2a). According to Bokov *et al.* (*12*), the spectrum may be divided into two quadrupole doublets: the first with an isomer shift δ_1 = 0.24 and a quadrupole splitting Δ_1 = 0.95 mm sec^{-1} relates to Fe^{3+} ions in the tetrahedral positions; the second with δ_2 = 0.36 and Δ_2 = 0.37 mm sec^{-1} corresponds to the octahedral Fe^{3+} ions. The isomer shifts are expressed with respect to α-Fe. By decreasing the temperature down to 77 K, a magnetic ordering can be observed, showing antiferromagnetic behavior below T_N = 265 K.

The Mössbauer spectra taken at 295 K for disks irradiated with doses ranging from 1×10^{11} to 5×10^{12} ions cm^{-2} are shown in Fig. 2. One can see that ion bombardment results in an additional paramagnetic fraction which exhibits itself as a doublet superposed on that of the tetrahedral pattern of the undisturbed matrix. The intensity of the doublet increases with dose as expected and its linewidth is somewhat widened for doses higher than 10^{12} cm^{-2}.

In order to determine the absolute fraction of the disk which has been rendered

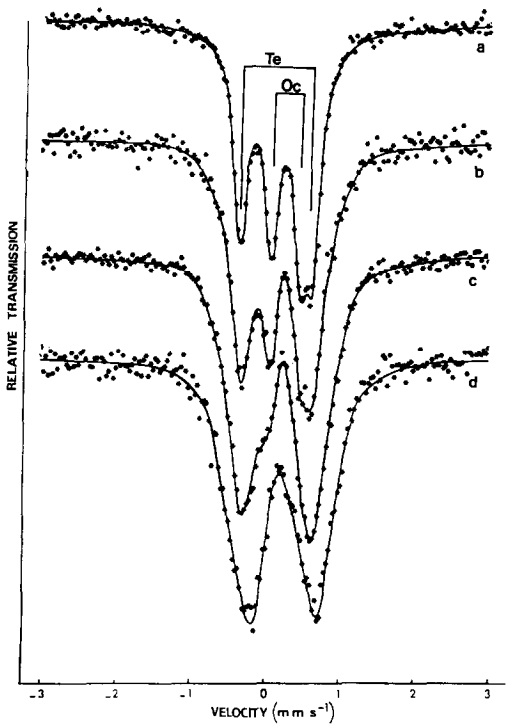

FIG. 2. ^{57}Fe Mössbauer spectra for $Bi_2Fe_4O_9$ at T = 295 K. (a) Nonirradiated sample; (b, c, d) 3.1 GeV–Xe irradiated samples for doses equal to 5×10^{11}, 1.2×10^{12}, and 5×10^{12} cm^{-2}, respectively.

paramagnetic by ion bombardment, the observed spectra were least-squares fitted with two doublets for doses between 1.5×10^{11} and 2.5×10^{12} cm^{-2} (Table I).

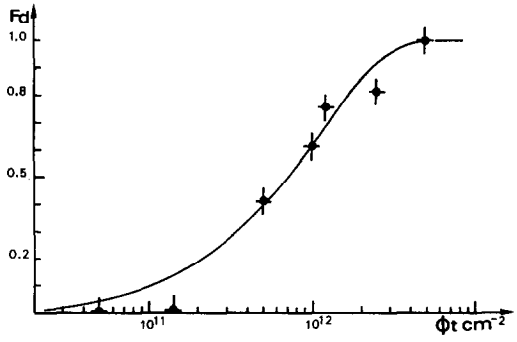

FIG. 3. Dose dependence of the paramagnetic fraction Fd induced by 3.1 GeV–Xe ions in $Bi_2Fe_4O_9$. The solid line has been calculated from Fe = 1 − $\exp(-\pi R^2 \phi t)$ with R = 5.5 nm.

The fits show that tetrahedral sites are increasingly favored with dose to the detriment of octahedral positions. As a consequence owing to the equal extent of Fe^{3+} ions in the tetrahedral and octahedral positions in the remaining undisturbed part of the target, the difference between the tetrahedral and octahedral contributions has been regarded as representing the paramagnetic fraction Fd produced by the incoming xenon ions. The values of Fd have been plotted versus dose ϕt in the Fig. 3.

TEM Observations

Electron diffraction is essential for characterization of the lattice state, degree of

TABLE I

MÖSSBAUER PARAMETERS OF $Bi_2Fe_4O_9$ SAMPLES IRRADIATED BY 3.1 GeV–Xe IONS

	Oc				Te			
ϕt (cm^{-2})	$\delta(\pm1)$	$\sigma(\pm2)$	$\Delta(\pm1)$	$\%(\pm3)$	$\delta(\pm1)$	$\sigma(\pm2)$	$\Delta(\pm1)$	$\%(\pm3)$
0	0.36	0.23	0.37	49	0.24	0.23	0.95	51
1.5×10^{11}	0.36	0.26	0.38	49	0.24	0.26	0.98	51
5×10^{11}	0.35	0.24	0.39	29	0.26	0.38	0.97	71
1.2×10^{12}	0.35	0.22	0.47	13	0.28	0.48	0.97	87
2.5×10^{12}	0.33	0.24	0.47	10	0.29	0.48	0.99	90
5×10^{12}					0.31	0.56	0.93	100

Note. δ(mm sec^{-1}) = Isomer shift relative to metallic iron. σ(mm sec^{-1}) = Half-height width of the lines (assuming a Lorentzian shape). Δ(mm sec^{-1}) = Quadrupole shift.

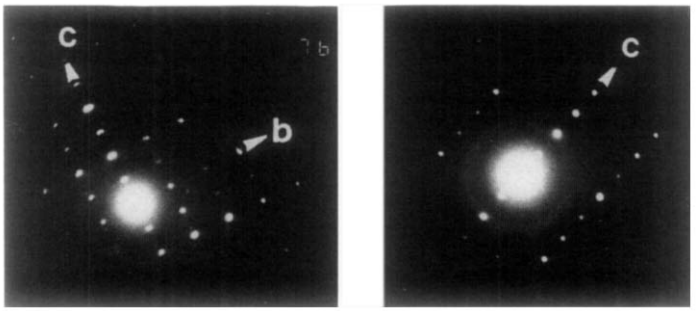

FIG. 4. ED patterns of specimens showing the coexistence of crystalline portions and amorphous ones.

metamictization, and mechanisms involved at different stages of radiation damage. Previous results reported for $BaFe_{12}O_{19}$ and $Y_3Fe_5O_{12}$ (*1–2*) irradiated by 1.8 GeV–Ar and 2.7 GeV–Kr ions showed that induced structural changes ranging from small defects to amorphization might indeed be revealed on the ED patterns.

For this reason, numerous microcrystals of $Bi_2Fe_4O_9$ were examined by electron diffraction and imaging at 250,000 magnification. Although a classification cannot be strictly defined, the observed ED patterns were arranged as follows to represent a possible sequence by which radiation damage is effected in $Bi_2Fe_4O_9$:

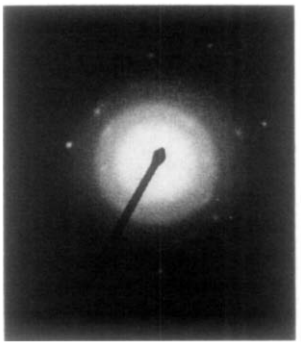

FIG. 5. ED patterns of specimens showing a complete destruction of the structure with the appearance of an amorphous state.

(i) Coexistence of crystalline portions, characterized by well-defined sharp spots, and amorphous areas characterized by the presence of broad halo-rings (Figs. 4a and 4b). Reconstructing the reciprocal space of such crystals led, as expected, to the orthorhombic cell of $Bi_2Fe_4O_9$ and to reflection conditions consistent with the space group *Pbam* (*11*).

Unlike $BaFe_{12}O_{19}$ irradiation by Ar or Kr ions (*5–7*), it is worth noting that the diffraction spots are well resolved without streakings due to lattice strain.

(ii) Complete destruction of the structure with the appearance of an amorphous state (Fig. 5). It should be remarked that diffuse weak spots or weak dotted rings are observed in the halo-rings.

(iii) Further radiation damage of the amorphous material associated with the occurrence of Debye rings, i.e., crystallized microdomains (Fig. 6).

This sequence was confirmed by the bright and dark field images. As a matter of fact, the characteristic images consist of dark and bright arrays in either a speckled or a striped arrangement. Such a feature is related to the direction of the Xe ion beams with respect to the crystal since polycrystalline state of the sample allows the particles to be oriented at random. However, it must be mentioned that the stripe widths

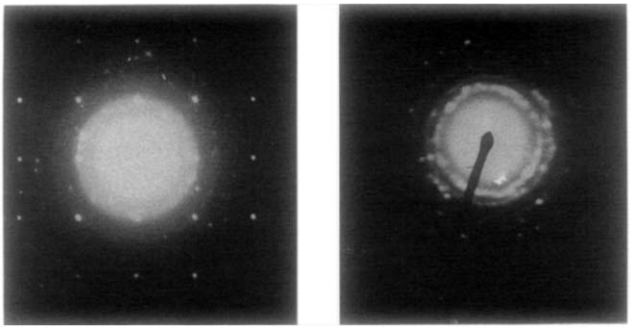

a b

FIG. 6. Further radiation damage of the amorphous material leads to ED patterns characteristic of crystallized microdomains.

are highly variable from one crystal to the other and within the bulk of the crystals. This leads to a problem in the interpretation of the image contrast. Figure 7 shows a low resolution image which exhibits the typical striped contrast, with bright areas indicated by A in the figure and dark ones by C. The corresponding diffraction pattern of Fig. 7b (zone axis [001]) shows the sharp spots of the basis cell ($h00$) and $0k0$ spots with $h = 2n + 1$ and $k = 2n + 1$ are observed, owing to multiple diffraction phenomena), and the halos previously described. The dark field image shown in Fig. 7c was made by selecting reflection labeled (a); the dark areas in Fig. 7a, and the corresponding bright ones in Fig. 7c (see the arrow) are crystalline areas of the matrix. This is clearly shown in the enlargement of the image (Fig. 8a) or in Fig. 8b where the 4.2 Å fringes associated with the reflection (111) appear in the dark part of the crystal edge.

Considering a direction that we assumed parallel to the Xe ion beam, crystals appear as speckled bright circular areas or as mosaic when the high density of such areas led to overlapping. An example is shown in Fig. 9a. The corresponding electron diffraction pattern (Fig. 9b) exhibits, as usual, the sharp spots of reflections (110) and the halo. The dark field image with the aperture in arrowed position (200) reveals the outer part of the circular areas, as shown in Fig. 9c.

Therefore it appears that for the samples exhibiting the ED patterns of type (i), the amorphization (metamictization) proceeds through the destruction of the lattice in the path of the Xe ions that form the latent tracks. They correspond to the bright arrays of the crystals in the bright field images.

Isolated latent tracks have been visualized in some parts of the crystal as continuous cylinders of amorphous like structures (Fig. 10) with a mean diameter of about 12 nm. However, it should be mentioned that one usually observed an extensive overlap of the tracks as expected for a fluence of 10^{12} ions cm^{-2}. These results explain the variable widths of the stripes which can indeed be considered as the projected images of statistically overlapped tracks. They are thus a function of the track density, the crystal thickness, and the direction of the electron microscopy observations.

The second type of electron diffraction pattern encountered in our sample (ii) exhibits broad rings with small spots in the inner part. The corresponding dark field images show the microcrystalline character of the matrix (Fig. 11a), the circle labeled (a)

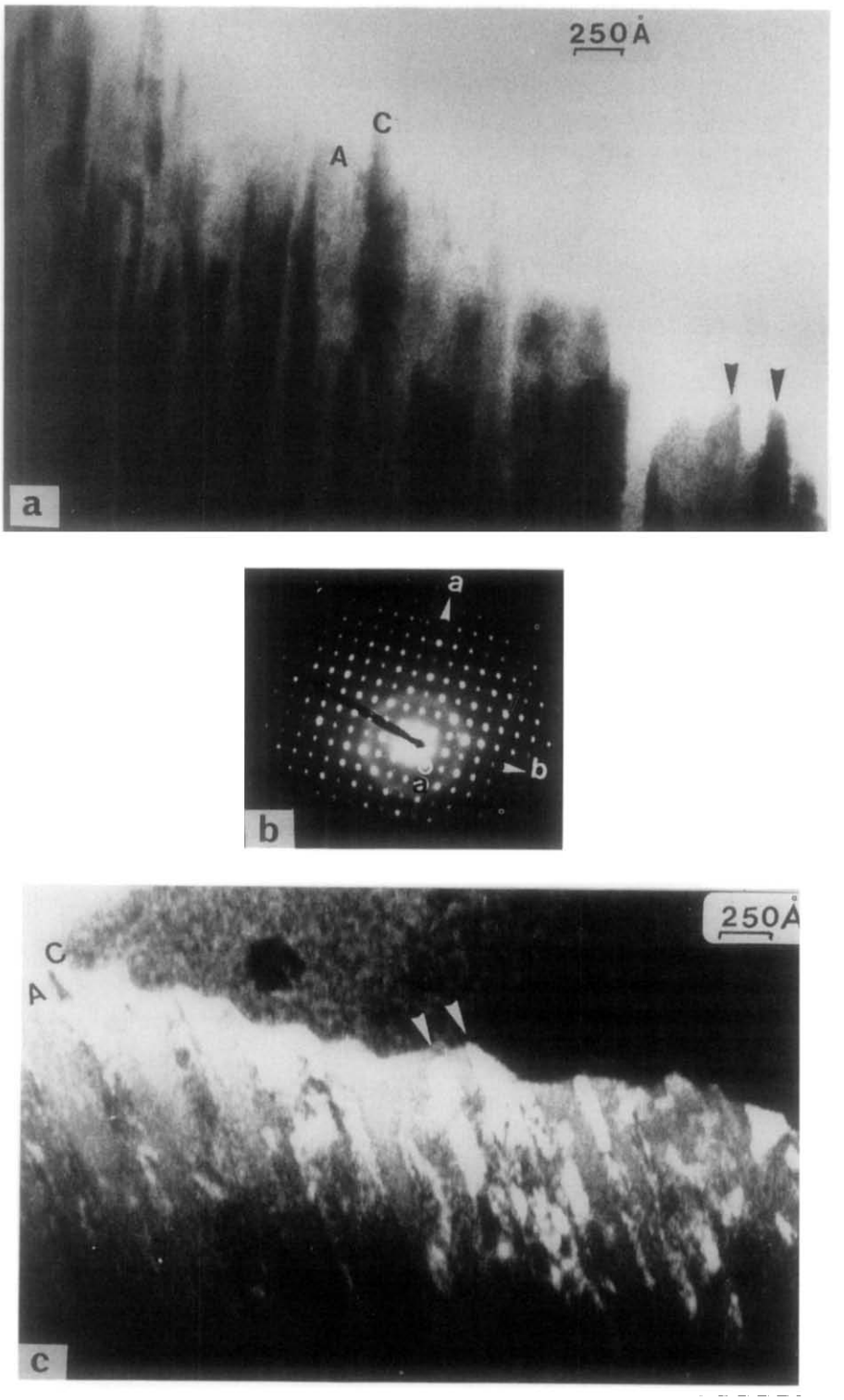

FIG. 7. (a) Bright field image [001] of a stripped crystal. Dark areas are labeled C and the bright ones A. (b) Electron diffraction pattern. (c) Dark field image (selected reflection ($\bar{1}10$)) of the same area.

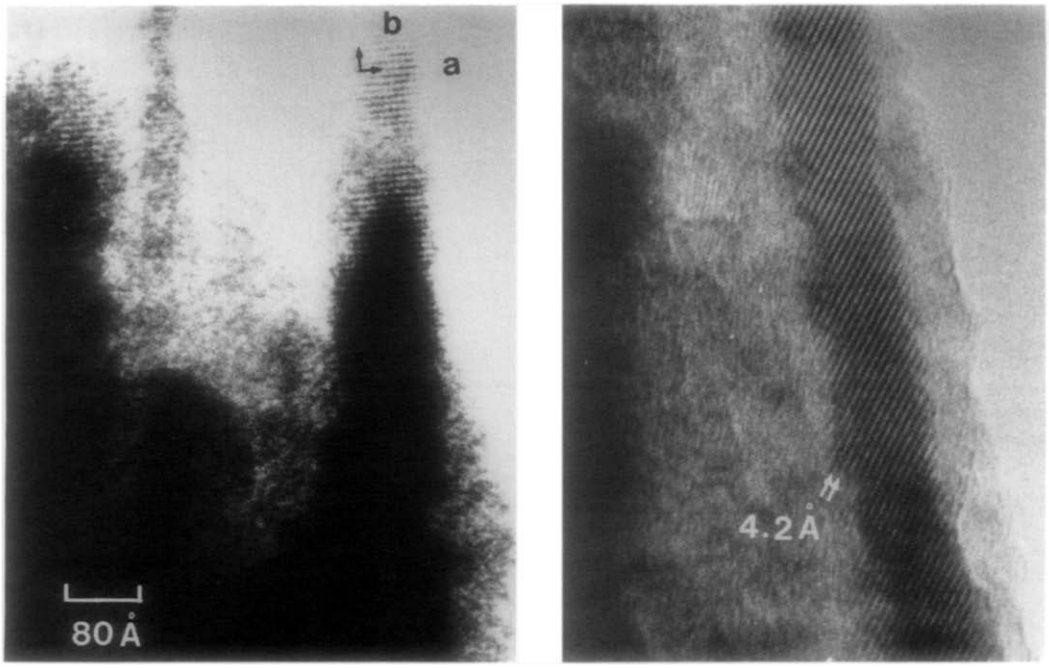

FIG. 8. The dark areas are crystalline: (a) enlarged image of areas A and C of Fig. 7a. (b) Fringes associated with the reflection (111).

shows the selected area of the electron diffraction pattern (Fig. 11b). The diameter of the small crystallites is about 2 nm. Intense electron beam heating induces a rapid change in such specimens: rings become sharper as the crystallites grow. An example is shown in Fig. 11c where the mean diameter of the crystallites is now about 15 nm. The examination of specimens which correspond to the beginning of the recrystallization process shows that the grains are then ill-defined and could be better interpreted as crystallized domains. The high resolution micrograph in Fig. 12 shows that the fringes are often wavy and strongly disturbed and the domains never exhibit narrow boundaries. Although no systematical preferred orientation was observed as previously reported for the barium ferrite (*8*) the rings (200) and (022) are always the most intense, and numerous domains exhibit such lattice fringes.

It must be pointed out that these phenomena only occur under electron irradiation when diffuse spots or rings are already evident in the broad ring. Thus, they were never observed in the particles of type (i). Next a systematic investigation of the sharp ring pattern was carried out in order to characterize the nature of the grain.

Taking into account the experimental error caused by the width of the rings, related to the experimental conditions and the crystallite size, the calculated reticular spacings agree with those of $Bi_2Fe_4O_9$. However, it should be noted that forbidden reflections such as (011) or (101) are often observed in the ring patterns; this feature

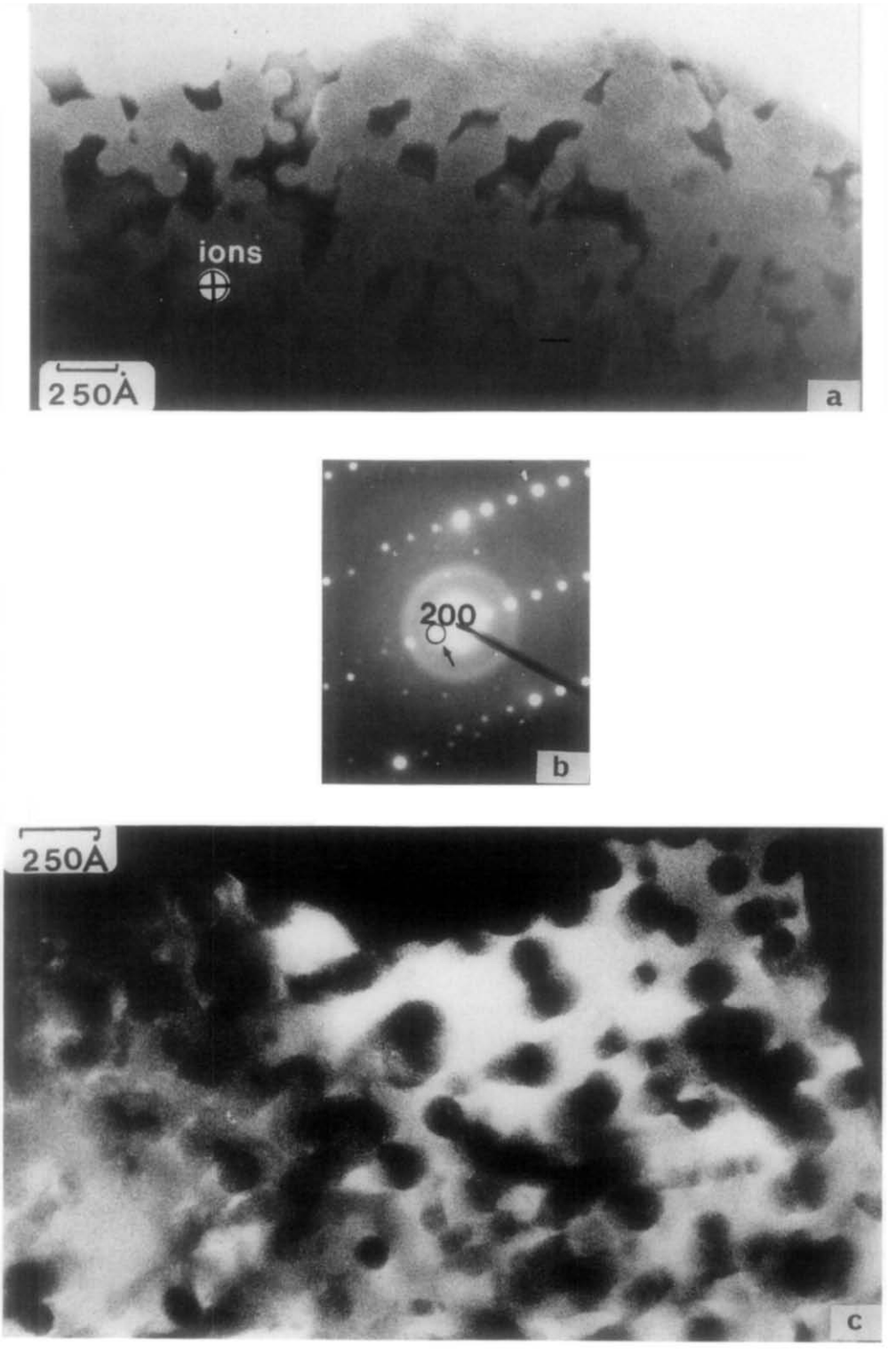

FIG. 9. Bright field (a) and dark field (c) images corresponding to a part of the (200) ring (b).

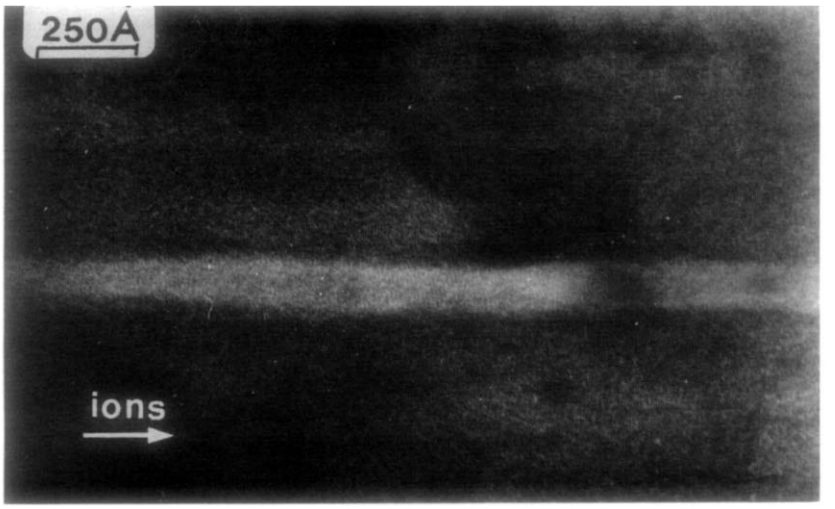

FIG. 10. Lattice image of a 3.1 GeV–Xe latent track in $Bi_2Fe_4O_9$.

could be imputed either to a loss of symmetry or better, as we assume, to multiple diffraction phenomena.

Such rings, correlated with the occurrence of crystallized microdomains are sometimes associated with the spots characteristic of $Bi_2Fe_4O_9$; they correspond to the third group of specimens. The dark field image in Fig. 13b was obtained from the selected area labeled (a), including parts of the rings (220) and(022) and (310) reflection. We observe the bright part of the residual crystalline matrix (arrowed) and small microcrystals arising in the noncrystalline part of the bulk. This type of specimen exhibits exactly the same behavior with the electron irradiation intensity.

Discussion and Conclusion

As reported for $Y_3Fe_5O_{12}$ and $BaFe_{12}O_{19}$ (*10–13*), the irradiation of $Bi_2Fe_4O_9$ with 3.1 GeV–Xe ions leads to the creation of nuclear tracks. Therefore the dose dependence of the paramagnetic fraction deduced from the Mössbauer spectra can be described by the exponential law (*14*):

$$Fd = 1 - \exp(-\sigma_{(RP)}\phi t).$$

The cross section of the paramagnetic cylinders built up around the path of the Xe ions is $\sigma_{(Rp)} = \pi Rp^2$ where Rp will be taken as the paramagnetic radius. From the Fig. 3, we find $Rp = 5.5$ nm with a standard deviation estimated to about 0.5 nm. The value is in fair agreement with that measured on the HREM micrographs (*15*).

The induced paramagnetic and nearly amorphous phase is characterized by Mössbauer parameters $\delta = 0.31$ mm sec^{-1} with respect to α – Fe and $\Delta = 0.93$ mm sec^{-1}. The value of the isomer shift is practically the average value of IS in the unperturbed $Bi_2Fe_4O_9$ and does not allow a conclusion to be reached concerning the actual structure of the immediate surrounding of the Fe^{3+} ions in the irradiated matrix. Nevertheless, it should be pointed out that the ED patterns related to specimens of the third group (Fig. 6b) reveal Debye rings consistent with (220) and (022) reflections of $Bi_2Fe_4O_9$. This result suggests that a peculiar memory of the initial state has been retained as it has been postulated for $BaFe_{12}O_{19}$ (*8*).

In order to elucidate the nature of the induced paramagnetic phase the tempera-

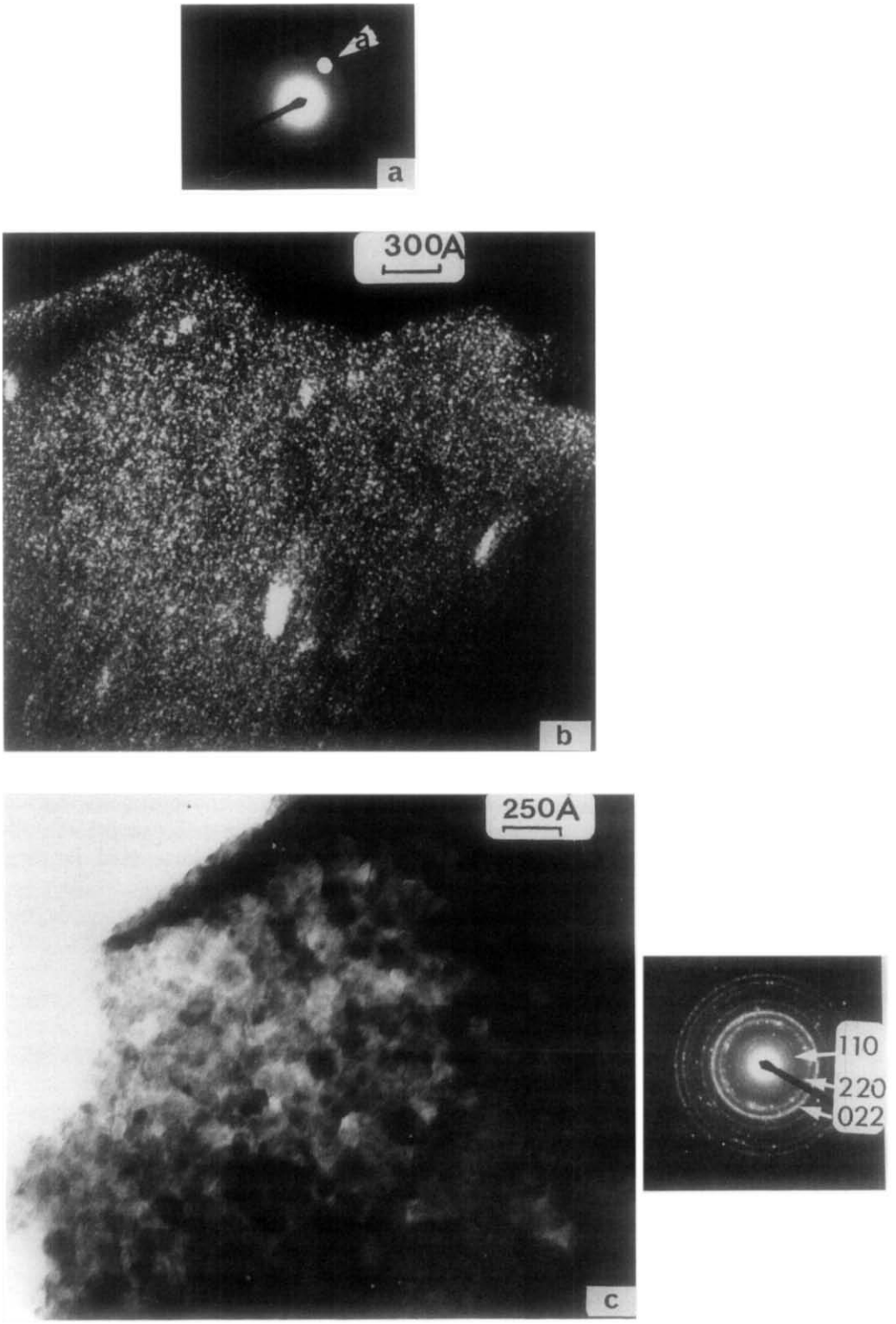

FIG. 11. Dark field image (b) of specimens exhibiting ED patterns (a) similar to Fig. 5. A strong electron beam heating induces a rapid change in size of the crystallites (c).

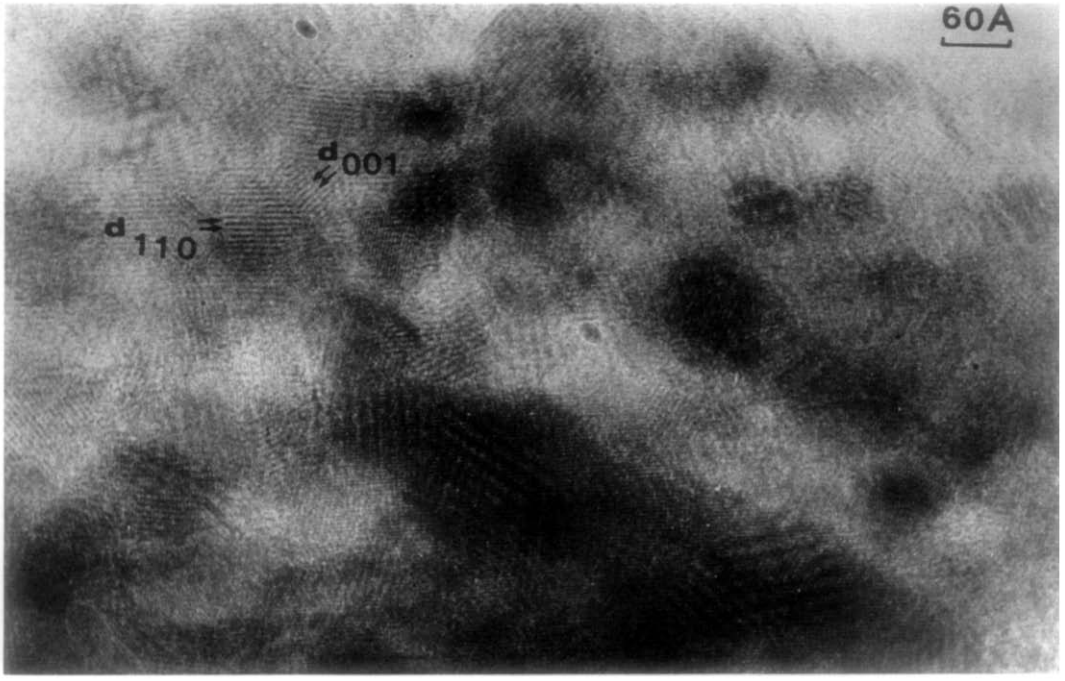

FIG. 12. High resolution micrograph of a fragment characterized by a recrystallization of a part of the amorphous matrix.

ture dependence of the Mössbauer spectra should be measured and compared with that of unirradiated samples. Furthermore, the amorphization (metamictization) of the target sets the problem of the track formation mechanism in this structure. A detailed study of those tracks by high resolution electron microscopy will allow this problem to be discussed in a later paper.

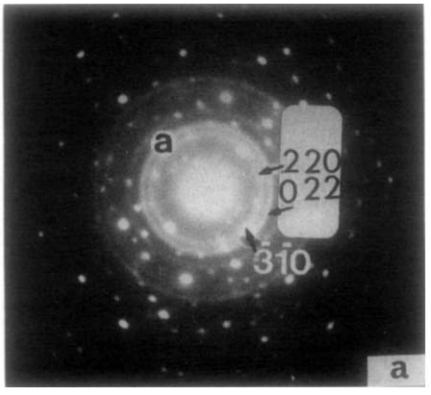

FIG. 13. ED pattern (a) and dark field image (b) of a specimen corresponding to further radiation damage of the amorphous material.

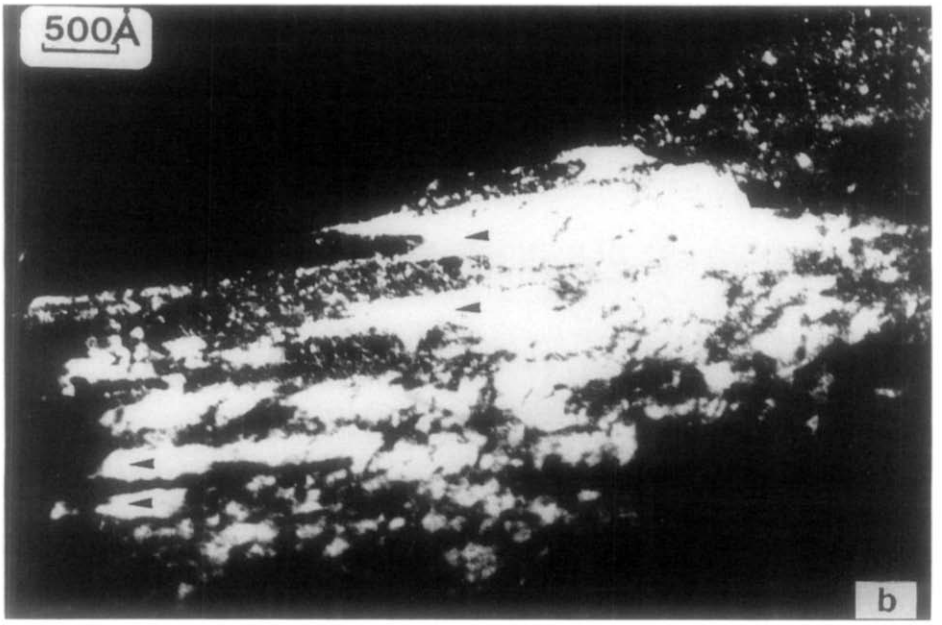

FIG. 13—*Continued.*

References

1. D. GROULT, M. HERVIEU, N. NGUYEN, B. RAVEAU, G. FUCHS, AND E. BALANZAT, *Rad. Effects* **90,** 191 (1985).
2. G. FUCHS, F. STUDER, E. BALANZAT, D. GROULT, J. C. JOUSSET, AND B. RAVEAU, *Nucl. Inst. Meth. B* **12,** 471 (1985).
3. F. STUDER, N. NGUYEN, G. FUCHS, AND M. TOULEMONDE, *Hyperf. Int.* **29,** 1287 (1986).
4. F. STUDER, D. GROULT, N. NGUYEN, AND M. TOULEMONDE, *Nucl. Inst. Meth. B* **20,** 856 (1987).
5. M. HERVIEU, D. GROULT, B. RAVEAU, AND G. FUCHS, *J. Solid State Chem.* **62,** 261 (1986).
6. M. HERVIEU, D. GROULT, AND B. RAVEAU, *Phys. Stat. Solid. (a)* **94,** 467 (1986).
7. M. HERVIEU, *J. Microsc. Spectrosc. Electron.* **10,** 159 (1986).
8. M. HERVIEU, D. GROULT, AND B. RAVEAU, *Rad. Effects* **97,** 75 (1986).
9. G. FUCHS, F. STUDER, E. BALANZAT, D. GROULT, M. TOULEMONDE, AND J. C. JOUSSET, *Europhysics Lett.* **3,** 321 (1987).
10. M. TOULEMONDE, G. FUCHS, N. NGUYEN, F. STUDER, AND D. GROULT, *Phys. Rev. B* **35,** 6560 (1987).
11. N. NIIZEKI AND M. WACHI, *Zeit. Kristallogr. B* **127,** 173 (1968).
12. V. A. BOKOV, G. V. NOVIKOV, V. A. TRUKHTANOV, AND S. I. YUSHCHUK, *Sov. Phys. Solid State* **11,** 2324 (1970).
13. G. FUCHS, D. GROULT, M. HERVIEU, N. NGUYEN, F. STUDER, M. TOULEMONDE, AND B. RAVEAU, *in* "Proceedings of the Third European Conference on Solid State Chemistry, Rogensburg, 1986."
14. P. HANSEN, H. HEITMANN, AND P. M. SMIT, *Phys. Rev. B* **26,** 3539 (1982).
15. D. GROULT, M. HERVIEU, N. NGUYEN, AND B. RAVEAU, *J. Solid State Chem.* **76,** 260 (1988).